Zitierweise: *Angew. Chem. Int. Ed.* **2022,** *61,* e202202561
Internationale Ausgabe: doi.org/10.1002/anie.202202561
Deutsche Ausgabe: doi.org/10.1002/ange.202202561

Single-Atom Catalysis

Adatom Bonding Sites in a Nickel-Fe_3O_4(001) Single-Atom Model Catalyst and O_2 Reactivity Unveiled by Surface Action Spectroscopy with Infrared Free-Electron Laser Light

Yun Liu[+], Zhongkang Han[+], Sandy Gewinner, Wieland Schöllkopf, Sergey V. Levchenko, Helmut Kuhlenbeck,* and Beatriz Roldan Cuenya*

Abstract: Single-atom (SA) catalysis presently receives much attention with its promise to decrease the cost of the active material while increasing the catalyst's performance. However, key details such as the exact location of SA species and their stability are often unclear due to a lack of atomic level information. Here, we show how vibrational spectra measured with surface action spectroscopy (SAS) and density functional theory (DFT) simulations can differentiate between different adatom binding sites and determine the location of Ni and Au single atoms on Fe_3O_4(001). We reveal that Ni and Au adatoms selectively bind to surface oxygen ions which are octahedrally coordinated to Fe ions. In addition, we find that the Ni adatoms can activate O_2 to superoxide in contrast to the bare surface and Ni in subsurface positions. Overall, we unveil the advantages of combining SAS and DFT for improving the understanding of single-atom catalysts.

Introduction

Catalysis plays an important role in many economically, socially, and environmentally relevant processes such as industrial chemical production, exhaust gas cleaning, corrosion, and many others.[1] Single-atom catalysis (SAC) is a frontier in the field of heterogeneous catalysis. A "single-atom catalyst" refers to a system where a small amount of material is highly dispersed on a support such that the dispersed atoms do not aggregate. Metal oxides are widely used as supports for SAC,[2,3] and it is well known that the binding interactions between surface oxygen anions and the dispersed single atoms are critical for the stabilization of the adatoms.[2,4,5] There are often several inequivalent types of surface oxygen anions available for bonding, but it is commonly not known to which type of anion the adatoms bind. However, this information is very important for the understanding of the catalytic reaction mechanism.[2,6]

Most single-atom catalyst studies have been performed for powder catalysts due to their more realistic nature and the more facile reactivity characterization, but such studies are hampered by the complex surfaces in such systems, which often prevent a precise structure determination. The structure of epitaxial thin-film catalysts is simpler, easier to control and easier to characterize,[7–12] and therefore a clearer understanding of the adatom-substrate interaction and the catalytic performance may be gained.

Oxygen anions are the preferred bonding partners for single-metal atoms, but few techniques can distinguish between different types of surface oxygen atoms.[13] They are difficult to detect with electron microscopy and X-ray scattering methods, which are two typical techniques employed to study SAC powder catalysts. Scanning tunneling microscopy (STM) is commonly used for the structural characterization of crystalline samples, but the interpretation of STM images is not straightforward since not only the surface atomic arrangement but also the electronic structure will determine the image contrast. Moreover, adatoms will dominate the contrast in STM images because of their larger height, which renders the analysis of the SA binding sites challenging. Sometimes the simulation of STM images with DFT may help, but the significance may be limited if part of the atoms is invisible in the STM images.

Surface action spectroscopy (SAS) is a novel surface-sensitive vibrational technique employing infrared free-electron laser radiation.[14–17] In combination with DFT

[*] Y. Liu,[+] H. Kuhlenbeck, B. Roldan Cuenya
Department of Interface Science, Fritz-Haber Institute of the Max Planck Society
Faradayweg 4–6, 14195 Berlin (Germany)
E-mail: yliu@fhi-berlin.mpg.de
kuhlenbeck@fhi-berlin.mpg.de

Z. Han,[+] S. V. Levchenko
Center for Energy Science and Technology, Skolkovo Institute of Science and Technology
Bolshoy Blvd. 30/1, 121205 Moscow (Russia)

S. Gewinner, W. Schöllkopf
Molecular Physics Department, Fritz-Haber Institute of the Max Planck Society
Faradayweg 4–6, 14195 Berlin (Germany)

[+] These authors contributed equally to this work.

simulations it can be employed to identify surface structures using the surface vibrational spectrum as a fingerprint of the surface atomic arrangement.[15,17] Here, we apply this approach to elucidate the location of single atoms on their support by comparison of measured SAS spectra with vibrational spectra simulated with DFT for different single-atom bonding sites.

Fe–Ni mixed oxides are promising catalysts for the oxygen evolution reaction (OER),[18,19] and therefore we have selected $Fe_3O_4(001)$ with Ni adatoms to demonstrate the suitability of this approach. The $(\sqrt{2}\times\sqrt{2})R45°$ surface reconstruction of $Fe_3O_4(001)$ has been studied with IV-LEED, which revealed that it is caused by a rearrangement of the iron-sublattice, leading to subsurface cation vacancies (SCVs).[20] Au adatoms adsorb at the same surface sites as Ni adatoms according to previous STM studies,[21,22] but the layer structure is simpler, which is why we included them in this study for reference purposes. For both types of adatoms, the STM images do not directly reveal the surface oxygen bonding partners,[20,21,23] but based on DFT energy calculations and structural reasoning it was argued that the adatoms are "twofold coordinated to surface oxygen where there is no subsurface Fe_{tet} neighbor",[20,21,23] with Fe_{tet} being a tetrahedrally coordinated iron ion. A direct experimental proof of this statement was not given. Ryan et al. have studied Ni atom on $Fe_3O_4(001)$ with NIXSW (normal incidence X-ray standing wave) and report that the Ni adatoms are located at "bulk-continuation tetrahedral sites".[24] This terminology does not consider the SCV surface reconstruction and therefore cannot consider all the different types of surface sites induced by the reconstruction.

There are three types of symmetrically inequivalent oxygen ions at the SCV-reconstructed $Fe_3O_4(001)$ surface. Using STM, DFT and SAS we show that the Ni and Au adatoms form bridging bonds to those oxygen ions which are coordinated to octahedral Fe cations only. These are the sites suggested in preceding publications,[20–23] but without direct experimental proof. In contrast to Ni at subsurface positions, surface Ni adatoms can activate O_2 molecules to superoxide already below room temperature, making this system interesting for low-temperature oxidation catalysis.

Results and Discussion

Adatom Binding Sites on $Fe_3O_4(001)$

We have prepared thin $Fe_3O_4(001)$ films with a thickness between 8 and 12 nm on Pt(001) using well-established recipes.[25] In the following discussion, Fe_{oct} refers to iron ions which would be octahedrally coordinated in the bulk. At the very surface the coordination is smaller, but these Fe ions are commonly still called "octahedrally coordinated". In a similar way, Fe_{tet} refers to iron ions which would be tetrahedrally coordinated in the bulk. The $Fe_3O_4(001)$ thin film surface structure is identical to that of $Fe_3O_4(001)$ single crystals according to STM and LEED results.[26] LEED shows the sharp $(\sqrt{2}\times\sqrt{2})R45°$ pattern of the subsurface cation vacancy (SCV) reconstruction, whose atomic structure has recently been revealed with IV-LEED.[20,26] Specifically, two octahedrally coordinated Fe_{oct} atoms in the third layer [we call this "(S-2)" in the following, which means two layers below the surface] are removed, and one tetrahedrally coordinated Fe_{tet} atom moves into the second layer [(S-1)] as an interstitial atom (Fe_{int}). This rearrangement creates a Fe cation vacancy and changes the Fe:O atomic concentration ratio in the topmost four layers from 12:16 to 11:16. The topmost surface layer consists of 4 Fe_{oct} cations and 8 oxygen anions in the $(\sqrt{2}\times\sqrt{2})R45°$ surface unit cell. Wiggling rows of protrusions resulting from the presence of the subsurface cation vacancies[20] dominate the high-resolution STM image in Figure 1a. The protrusions result from Fe cations which have a high electronic density of states near the Fermi level.[20,26] Some defects, e.g., surface OH groups, unreconstructed unit cells and antiphase domain boundaries show up with larger apparent heights than the regular sites in the STM images.[26] We estimate that the concentration of such defects is below 6 %.

Figure 1b depicts the positions of the three inequivalent kinds of surface oxygen ions at the surface. Four surface oxygen ions labeled O_u are coordinated to two surface Fe_{oct} ions and one Fe_{tet} ion in the (S-1) layer. The two oxygen ions O_i have a similar coordination environment but bind to an interstitial Fe_{int} ion instead of Fe_{tet}, and the remaining two oxygen O_z ions are coordinated only to Fe_{oct} ions, two in the surface layer [(S)], and one in the (S-2) layer.

STM does not directly reveal details about the position of the oxygen ions and therefore, we have used SAS in combination with DFT to elucidate the oxygen bonding environments of the metal adatoms at the surface. The central element of the approach is the surface vibrational spectrum of the oxide substrate covered with single atoms. This is measured with SAS and serves as a fingerprint of the surface structure.[14,17] DFT using the PBE+U approximation ($U=3.61$ eV) to the exchange-correlation functional[22] was employed to provide simulated surface vibrational spectra in the harmonic approximation for different single-atom coordination environments. Comparison of the experimental spectrum with the simulated ones reveals the single-atom adsorption site if the real structure is among those used for the vibrational simulations.

The computation of simulated SAS spectra requires to model the surface structure with DFT, which involves a structure optimization process. A structure determined with IV-LEED[20] served as starting structure for the optimization process. Finally, simulated SAS spectra were computed from the DFT-derived surface normal modes according to the procedure described in the Supporting Information. We note that the computed intensities are related to approximated infrared absorption coefficients, while the SAS intensities additionally depend on the messenger desorption mechanism,[15,16] which hampers a direct quantitative comparison of intensities between experiment and simulations.

Figure 1c compares an experimental SAS spectrum with a simulated one. The match is good for the intense vibrations, but some of the weaker intensities in the simulated spectrum are barely visible in the experimental

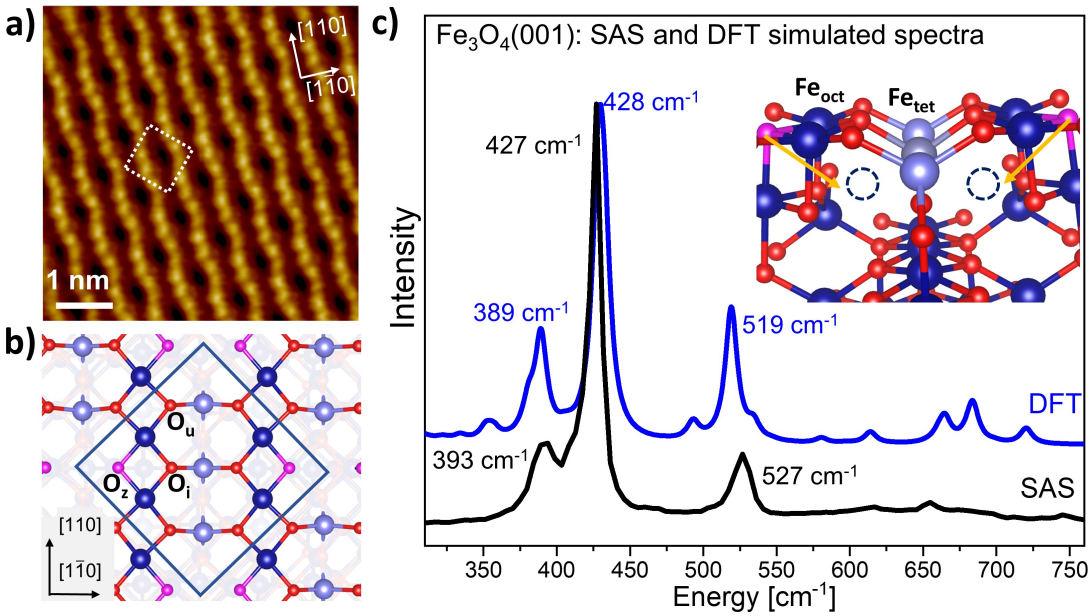

Figure 1. Structural and vibrational data for Fe_3O_4(001). a) high-resolution STM image of Fe_3O_4(001); scan parameters: sample bias (V) = 1.0 V, tunneling current (I) = 0.07 nA. The dotted square shows a ($\sqrt{2}\times\sqrt{2}$)R45° surface unit cell. b) Ball-stick model (top view) of Fe_3O_4(001). The three types of inequivalent surface oxygen atoms are labeled with O_z, O_u, and O_i. c) Comparison of an experimental and a DFT-simulated Fe_3O_4(001) SAS spectrum. The inset shows a side-view ball-stick model of Fe_3O_4(001) with subsurface cation vacancies (dashed open circles). The yellow arrows indicate the computed displacement amplitude of O_z atoms for the 519 cm^{-1} vibrational mode according to the DFT simulation (multiplied by a factor of 5), see Table S1 for some details of the modes. Color code: Fe_{oct}: blue; Fe_{tet}: purple; O_z atoms: pink; other oxygen atoms: red.

one, which may result from the limitations of the intensity calculation. Nevertheless, the agreement of the SAS spectrum with the modelled spectrum is reasonable, which supports the structural model derived in previous LEED-IV and SXRD studies.[20,27] We note that the computed surface vibrational normal modes and energies depend somewhat on the chosen slab. An example is discussed in the Supporting Information in the context of Figures S1 and S2.

Fe_3O_4(001) is a suitable substrate for the stabilization of Ni and Au single metal adatoms.[21–23] Figure 2a and b show STM images of a low coverage of Ni single atoms deposited at 300 K. Apparently, the Ni atoms are located at the "narrow" sites between the Fe_{oct} rows (see Figure 2a). The same was recently found with STM measurements for Au single atoms.[20,21] However, the oxygen atoms are not visible and therefore, the STM images do not directly reveal the oxygen bonding partners. Figure S3 shows STM images for higher Ni coverages, but also here STM does not reveal atomic details of the Ni adatom bonding sites. STM images of Fe_3O_4(001) single crystal surfaces and Ni adatoms on such surfaces as published by the Diebold and Parkinson group[18,22,23] are very similar to those shown in Figure 2a, which shows that Fe_3O_4(001) thin film and single crystal surfaces have very similar properties.

Table S2 lists DFT-derived binding energies for Ni adatoms on different surface oxygen sites; structure models are shown in Figure 2c–e. The adsorption energies of Ni adsorbed on O_z and O_i sites are similar (−3.14 eV for O_z and −2.94 eV for O_i), while the adsorption energy on an O_u site is significantly smaller (−2.07 eV). From these energies one would expect that the adatoms bind to O_z sites, but since DFT-derived energies usually have some uncertainty, an experimental proof for this finding would be profitable.

SAS spectra were recorded for Fe_3O_4(001) with different Ni coverages up to 1 ML. The complete set of data is shown in Figure S4. Figure 3a shows a sub-set. Curves i and iii in Figure 3a are spectra of pristine Fe_3O_4(001) and Fe_3O_4(001) with 1 ML Ni, respectively. Apparently, the band at 527 cm^{-1} is almost completely quenched after deposition of 1 ML of Ni, while the peaks at 393 cm^{-1} and 427 cm^{-1} are still visible, though the intensity of both peaks has decreased. The peak at 527 cm^{-1} becomes a double peak at 0.12 ML Ni (curve ii in Figure 3a) and broadens further at higher Ni coverages, see Figure S4. A similar effect is observed when Au adatoms are present, see Figure S5.

Simulated SAS spectra with Ni atoms bound to the three different oxygen surface sites are shown in Figure 3b, spectra ii–iv. The STM images in Figure 2 reveal that the adatoms occupy bridging positions and therefore only bridging bonding sites were considered in the simulations. Top-view ball-stick models of the structures are shown in Figure 2c–e and side views in Figure S6. In all cases, there was one Ni adatom per ($\sqrt{2}\times\sqrt{2}$)R45° surface unit cell (1 ML). Comparison of the computed spectra with the experimental spectrum, Figure 3b, spectrum iii, reveals that the agreement is best for the case that the Ni ions coordinate to O_z anions. In the simulation the intense mode at 428 cm^{-1} (SAS: 427 cm^{-1}) shifts only weakly, as also observed experimentally, and the mode at 519 cm^{-1} (SAS: 527 cm^{-1}) is completely quenched. In agreement with this, experimentally a strong quenching of the latter mode is observed with some remaining intensity due to layer imperfections dis-

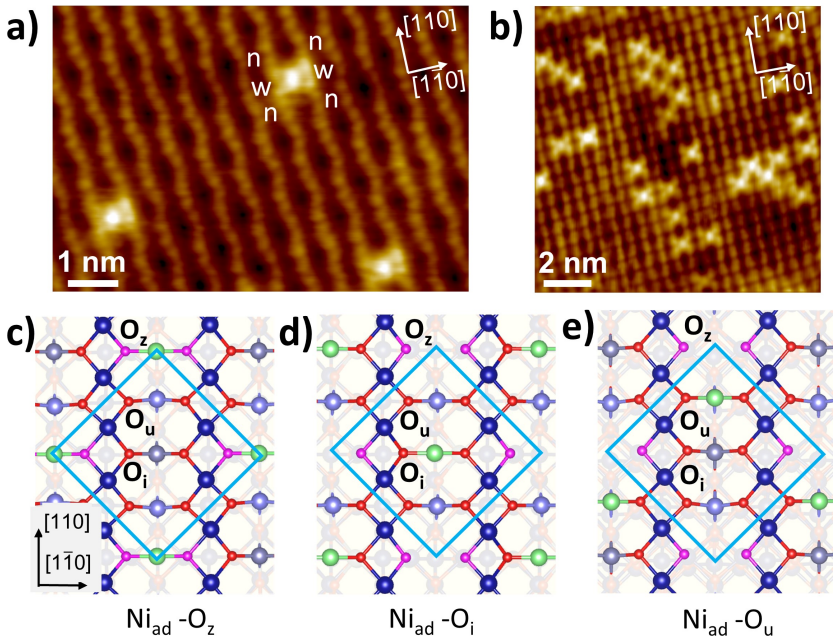

Figure 2. Experimental and theoretical data for single Ni atoms on Fe_3O_4(001). a) High-resolution STM image of Ni adatoms (0.06 ML) on Fe_3O_4(001)/Pt(001). The letters "n" and "w" indicate "narrow" and "wide" hollow sites between the wiggling Fe_{oct} rows, respectively. Scan parameters: $V = +1.0$ V, $I = 0.08$ nA. b) STM image of 0.20 ML Ni on Fe_3O_4(001). Scan parameters: $V = +1.0$ V, $I = 0.2$ nA. c)–e) Top-view ball-stick models for Ni bound to O_z, O_i, and O_u sites in bridging positions. Color code: Fe_{oct}: blue; Fe_{tet}: purple; O_z: pink; Other oxygen ions: red; Ni adatoms: green.

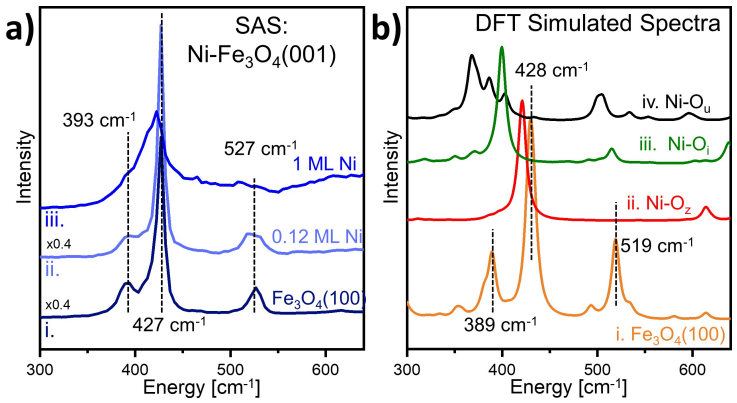

Figure 3. Comparison of SAS and DFT simulated spectra of Fe_3O_4(001) with and without Ni adatoms. a) Experimental SAS spectra of (i) pristine Fe_3O_4(001), (ii) 0.12 ML Ni and (iii) 1 ML Ni on Fe_3O_4(001). Ni was deposited at 300 K. b) DFT simulated spectra of (i) pristine Fe_3O_4(001), and (ii–iv) 1 ML Ni on Fe_3O_4(001) with the Ni atoms coordinated to different oxygen atoms. (ii) O_z, (iii) O_i, (iv) O_u (see Figure 2c–e).

cussed below. For the other sites the shift of the intense mode at 428 cm^{-1} (SAS: 427 cm^{-1}) is more pronounced and there is remaining intensity for the mode at 519 cm^{-1} (SAS: 527 cm^{-1}). Our result of Ni and Au single atoms binding to O_z sites is the first experimental verification of a previous prediction based mostly on DFT computed binding energies and structural reasoning based on STM images.[23]

We attribute the splitting of the 527 cm^{-1} peak in the SAS spectrum to the complexity of the Ni layer. The STM image shown in Figure 2b reveals that there are uncovered areas and Ni islands with Ni atoms having different numbers of Ni neighbors, i.e., the layer is structurally complex. The Ni coverage was smaller for the layer employed for SAS, but the situation is probably similar. We speculate that the splitting of the peak results from a superposition of components related to the inhomogeneous Ni distribution at the surface.

There is also a massive broadening of the intense mode at 428 cm^{-1} (SAS: 427 cm^{-1}) towards lower energies, which is not found in the simulations. We attribute this to the complexity of the Ni-covered surface. Ni coverages below 1 ML lead to complex layer structures with many different environments for the deposited Ni atoms (Figure S3). Ni island borders, one-dimensional Ni structures and isolated atoms (Figure S3) contribute intensity to the SAS spectra, while Ni atoms surrounded by other Ni atoms in all

directions may not, see spectrum iv in Figure 3. Furthermore, the surface is neither fully nor homogeneously covered with Ni atoms when the coverage reaches or even exceeds one monolayer (Figure S3). Bliem et al. report that part of Ni atoms are integrated into the surface already at room temperature,[23] which may also apply to the present case. SAS accounts for this complexity by the broad and complex structure developing in the energy range between $\approx$380 and $\approx$430 cm^{-1}.

Table S2 shows that the energy for Ni atoms at a subsurface position is smaller than the energies for surface positions, which provides a driving force for subsurface diffusion. A similar result has been obtained in previous studies.[23] Ni diffusion to subsurface positions induces a change of the SAS spectra of 1 ML Ni on $Fe_3O_4(001)$: when the surface is annealed at 426 K, the peak at 527 cm^{-1} is partially recovered (Figure S7); at higher temperatures it gets even more intense. There is a 8 cm^{-1} red shift with respect to the clean surface spectrum for temperatures of up to 650 K, which may be explained by the presence of the Ni atoms below the surface, where they occupy octahedral sites in the third layer (S-2) as proposed previously.[23] Annealing at 830 K shifts the peak back to the energy of the clean surface, which we attribute to a diffusion of the Ni atoms into deeper layers as also proposed previously.[23] At this temperature also the LEED pattern has fully recovered and is identical to that of the clean surface before Ni deposition (Figure S8).

Table S1 lists some surface mode parameters as derived from the experimental and theoretical data in Figure 1. For some modes one or two kinds of oxygen ions clearly dominate the oscillatory movement; the ions with the largest amplitude are named in the last column. In a simple view one may expect that adatom bonding to an oscillating atom affects the vibrational mode the more, the larger the oscillation amplitude of the atom in this mode is. This led us to check whether modes where a certain atom has a dominating vibrational amplitude can be used as sensors for bonding of adatoms to this atom. Such an approach could locate adatoms at the surface without performing a complete structural analysis. The computational effort would be greatly reduced since normal modes would only be required for the clean surface and not for surfaces with adatoms at different positions. From computed amplitudes (see also Supporting Information movies S1–S3) one may conclude that the 427 cm^{-1} mode might be a suitable sensor for the interaction of adatoms with O_u and O_z ions, the 393 cm^{-1} mode would be a sensor for adatoms interactions with O_i, and the 527 cm^{-1} mode should be sensitive to adatom interactions with O_z. Thus, adatoms interactions with O_z should affect the 527 cm^{-1} and the 427 cm^{-1} mode, the latter possibly to a somewhat smaller extent. The spectra shown in Figure 3a were employed to test this hypothesis. A small Ni coverage (0.12 ML) apparently induces a splitting of the 527 cm^{-1} mode, in agreement with the hypothesis. The 427 cm^{-1} mode is not much affected, but it appears that some intensity builds up at its low-energy side, filling the valley between the 427 and the 393 cm^{-1} modes. At 1 ML Ni the 527 cm^{-1} mode is essentially gone, and a wide structure has developed between $\approx$360 and $\approx$440 cm^{-1}. This is mostly in agreement with the test hypothesis, but as discussed before, much of this wide feature is probably due to a complex surface structure with Ni at different sites. The effect of adsorbed gold atoms is similar, see Figure S5. Again, 0.2 ML of Au adatoms induce a splitting of the 527 cm^{-1} mode, which agrees with the reported result that gold atoms bind to O_z sites.[20] However, in this case the minimum between the 427 and the 393 cm^{-1} modes is not filled up which we attribute to the lower complexity of the gold layer. Thus, the prediction is reasonably well fulfilled also for Au single atoms.

If we consider just the experimental data, then the sensor modes seem to be reasonably sensitive to adatoms. We have used the simulated spectra of 1 ML Ni on different oxygen sites (see Figure 3b) to also get an idea of the selectivity. As discussed above, the simulated curves may suffer somewhat from inaccuracies of the theoretical approach, but we assume that the general trend of the conclusions drawn below is valid. The simulation of Ni binding to O_z, Figure 3b(ii), shows a strong effect on the 519 cm^{-1} (exp: 527 cm^{-1}) mode, which becomes invisible as also observed in the experimental spectrum, see Figure 3b(iii), and a weak effect on the 428 cm^{-1} (exp: 427 cm^{-1}) mode, as predicted by the test hypothesis. However, the 389 cm^{-1} (exp: 393 cm^{-1}) mode is also mostly gone, which contradicts the hypothesis, since this mode is a sensor for Ni bonding to O_i. Also, Ni binding to O_i and O_u affects all spectral features, not just those which the hypothesis predicts. This means that the method is sensitive, i.e., in all cases the sensor mode is massively affected by the interaction with adatoms, but it is not sufficiently selective. We attribute this to the strong interaction with Ni atoms, which does not just modify the bond of the oxygen bonding partner to the atoms in its direct environment, but the electronic and geometric structure of the whole surface. The direct adatom bonding partner(s) may be affected most, but the rest of the surface-near atoms is also affected, though somewhat less in general. One may expect that the method works better in cases where the adatom interaction is more local, such as protruding surface atoms. Nevertheless, such an analysis could give a first hint about the adatom location, which could be helpful for further studies.

O_2 Activation by Ni Single Atoms on $Fe_3O_4(001)$

The chemical activity of the Ni single atoms was tested with O_2 adsorption experiments. Figure 4a compares TPD spectra of O_2 on clean $Fe_3O_4(001)$ and $Fe_3O_4(001)$ with 0.5 ML of Ni. Clean $Fe_3O_4(001)$ is apparently inert, in agreement with previous O_2-TPD results,[28] but the Ni covered surface binds O_2 more strongly, with O_2 desorption peaks at $\approx$240 K and $\approx$265 K. These temperatures correspond to desorption activation energies of 0.65 eV and 0.73 eV according to a Redhead analysis[29] assuming an attempt frequency of 10^{13} Hz. Repeating the spectra three times revealed that the Ni layer is stable with respect to O_2 adsorption at least on the time scale defined by the three TPD runs (Figure S9a).

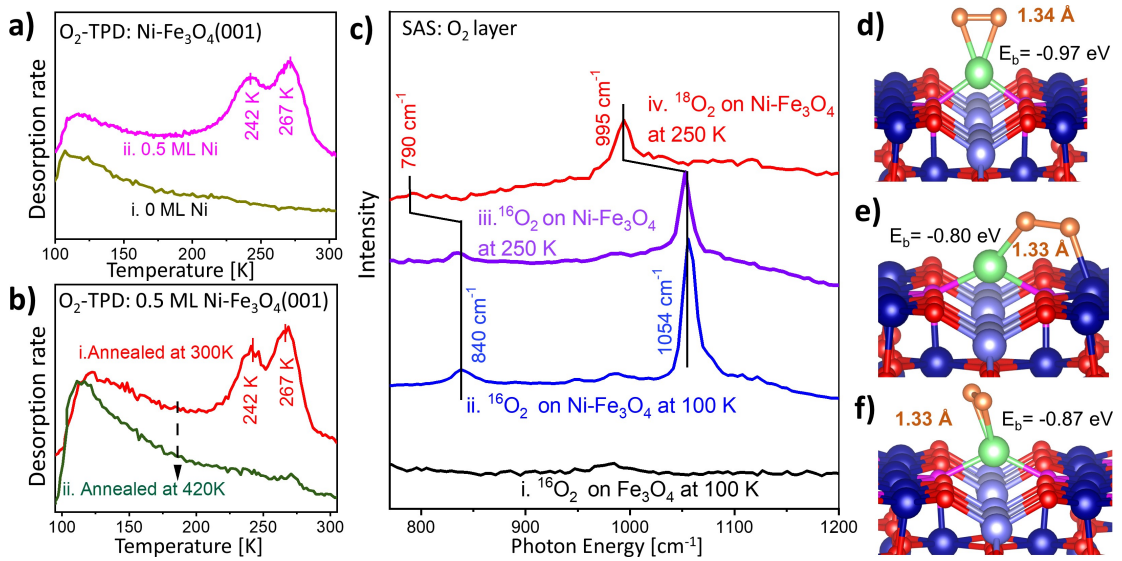

Figure 4. O_2 activation by Ni single atoms on Fe_3O_4(001). a) TPD spectra of O_2 adsorbed at 90 K on clean Fe_3O_4(001) and on Ni(0.5 ML)/Fe_3O_4(001). b) TPD spectra of O_2 adsorbed at 90 K on Ni(0.5 ML)/Fe_3O_4(001) after annealing at 300 K and 420 K. The heating rate was 2 K/s for all TPD spectra. c) SAS spectra of $^{16}O_2$ on clean Fe_3O_4(001) and Ni(0.4 ML)-Fe_3O_4(001) (i) $^{16}O_2$ on clean Fe_3O_4(001); ii) $^{16}O_2$ on Ni-Fe_3O_4(001); (iii) $^{16}O_2$ on Ni-Fe_3O_4(001) followed by annealing at 250 K; (iv) $^{18}O_2$ on Ni-Fe_3O_4(001) followed by annealing at 250 K. In all cases O_2 was dosed at 100 K. d)–f) DFT-optimized structures of the three most strongly adsorbed superoxide molecules on Ni-covered Fe_3O_4(001). O–O bond lengths and adsorption energies (E_b) are shown. Color codes: Fe_{oct}: blue; Fe_{tet}: purple; O_z: pink; other lattice oxygen atoms: red; Ni: green; adsorbed O_2: orange.

However, annealing at 420 K deactivates the surface (see Figure 4b), which we attribute to the diffusion of the Ni atoms into the (S-2) layer. Apparently, the subsurface Ni atoms cannot activate O_2.

The chemical nature of the adsorbed O_2 species was investigated with SAS vibrational spectroscopy. Figure 4c shows spectra for an energy range where the O–O stretching vibrations of superoxide and peroxide are expected. The data obtained after dosing O_2 to Fe_3O_4(001) without Ni, spectrum (i), shows only very weak peaks, which may be attributed to O_2 on not-yet identified defect sites. A small coverage of contaminations, possibly CO_2, may also be responsible for these signals. The Ni covered Fe_3O_4(001) surface binds much more O_2, see spectra (ii) and (iii). The peaks at 840 and 1054 cm^{-1} are attributed to peroxide and superoxide, respectively.[30–32] Spectrum (iv) was recorded with $^{18}O_2$ to verify that the observed peaks are due to O–O vibrations. In the $^{18}O_2$ spectrum peaks at 790 and 995 cm^{-1} are found, which correspond to those at 840 and 1054 cm^{-1} in the $^{16}O_2$ spectra according to the energy shift predicted by the harmonic approximation: $\nu(^{16}O_2)/\nu(^{18}O_2) = 1.06$.[33] The spectra (iii) and (iv) were measured after the O_2 layer had been quickly flashed to 250 K, a temperature between the two TPD peaks, see Figure 3a and b. At this temperature the part of the oxygen which desorbs in the low-temperature TPD peak has left the surface. The SAS peaks are apparently less intense due to the smaller O_2 coverage, but the vibrational energy did not change, indicating that the difference between the species is small (see Figure 4c, curve iii). After a flash to 310 K all O_2-related intensity had vanished as expected (not shown here).

Panels d-f in Figure 4 show the three PBE + U computed lowest-energy configurations of O_2 on Fe_3O_4(001) with Ni bound to O_z sites; Table S3 lists data for some additional configurations. Especially the computed superoxide vibrational energy in the second data row of Table S3 (1063.8 cm^{-1}) agrees well with the measured energy of 1054 cm^{-1}, see Figure 4c, but the other computed superoxide vibrational energies are not so much different that the energies could be used for a safe identification of the O_2 configuration at the surface. The computed superoxide adsorption energies (−0.8 to −0.97 eV, see Figure 4d–f) are roughly in agreement with the desorption activation energies obtained using the Redhead equation (0.65 eV and 0.73 eV). Only a loose agreement is expected since the Redhead equation uses a generic attempt frequency (10^{13} s^{-1}) and since the DFT-computed values are binding energies, while the Redhead equation computes desorption activation energies. There is probably also an unidentified contribution from the peroxide in the TPD spectra, but we assume the peroxide coverage is small as concluded from the small peroxide intensity in the SAS spectra. In all computed configurations, the O_2 molecules are in a superoxide state as concluded from the bond length. The computed adsorption energy of O_2 on Fe_3O_4(001) with Ni in subsurface positions (−0.38 eV) is smaller than those for Ni adatoms according to Table S3, which explains why oxygen desorption peaks were not found above 100 K in the TPD spectrum recorded after the surface had been annealed at 420 K, see Figure 4b.

Bader charges[34] (Q) for the Ni atoms before and after O_2 adsorption are listed in Table S4. The Ni adatoms on O_z sites bond directly to the O_2 molecules and therefore they exhibit larger charge state changes than the sub-surface Ni

atoms. As one may expect, not all the charge transferred to the oxygen molecule does come from the Ni atoms as shown by the non-vanishing sums of the $Q(O_2)$ and $\Delta Q(Ni)$ values in Table S4. This means that charge is supplied also by the iron and oxygen ions in the neighborhood.

The bonding site of the peroxide species remains an open topic. Increasing the Ni coverage to beyond one monolayer did not lead to a more intense peroxo SAS peak (not shown here), which indicates that the peroxide is not related to Ni aggregates. DFT found peroxide with a binding energy of −1.56 eV and an O–O bond length of 1.46 Å on a surface with oxygen vacancies (see Figure S10). The computed vibrational energy of this state (854 cm^{-1}, see Figure 4c) is similar to the measured one (840 cm^{-1}, see Table S3). However, it was argued that oxygen vacancies are not stable at the $Fe_3O_4(001)$ surface.[26] According to the DFT results, the surface oxygen vacancy formation energy for $Fe_3O_4(001)$ is significantly lowered by Ni in the (S-2) layer (3.8 eV→2.05 eV), which may result in a higher concentration of vacancies formed by annealing in UHV. Also, desorption of H_2O via recombination of two contaminating surface OH groups would leave a vacancy behind. At present, we cannot definitely assign the formation of peroxide to a certain surface feature, but we note that the intensity of the peroxide peak in Figure 4c is always much smaller than that of the superoxide peak, which might indicate that the peroxide coverage is small.

The high reactivity of the Ni-$Fe_3O_4(001)$ surface for O_2 activation to superoxide emphasizes the potential of SAC sites to achieve enhanced catalyst performances, which motivates future studies of the relationship between the structure of SAC sites on metal oxides and their associated O_2 reaction energetics.[30,32,35,36] Future work will also be devoted to a better understanding of the SAS mechanism and a theoretical description of how the adatom to surface bond affects the surface vibrational spectrum.

Conclusion

We applied a combination of SAS experiments and DFT simulations to elucidate the location of Ni and Au single atoms on $Fe_3O_4(001)$ using a fingerprinting approach. Due to the SCV reconstruction, there are three inequivalent types of lattice oxygen ions at the $Fe_3O_4(001)$ surface. We showed that Ni adatoms bind to O_z sites, verifying a hypothesis published some time ago based on DFT results and structural reasoning based on STM images. Additionally, we found that the Ni adatoms can activate O_2 to superoxide, while clean $Fe_3O_4(001)$ and $Fe_3O_4(001)$ with subsurface Ni are inactive.

We demonstrate that SAS vibrational fingerprinting is a useful method to identify the location of single atoms on a surface, which is relevant for improving the understanding of single-atom catalysts. We also tested a simplified approach where we used vibrational modes as detectors for adatom bonding sites but found that the sensitivity is reasonable while the selectivity is insufficient. In any case, advanced theoretical modelling, novel synthetic methods, operando spectroscopic information describing the evolution of SAC materials under reaction conditions and kinetic data will additionally be required. We see the method illustrated here as one component of the major effort that needs to be undertaken to shed light into the origin of the unusual activity and selectivity trends reported for single-atom catalysts.

Acknowledgements

We thank Prof. Gareth S. Parkinson, Dr. Matthias Meier and Dr. Xunhua Zhao for fruitful discussions. Yun Liu thanks the Alexander von Humboldt foundation for the postdoctoral fellowship. Financial support from the Deutsche Forschungsgemeinschaft (DFG, German Research Foundation)—project no. 388390466—TRR 247, subproject A4 and Germany's Excellence Strategy—EXC 2008—390540038—UniSysCat. is also greatly appreciated. The DFT calculations were supported by Russian Science Foundation grant 21-13-00419. Open Access funding enabled and organized by Projekt DEAL.

Conflict of Interest

The authors declare no conflict of interest.

Data Availability Statement

The data that support the findings of this study are available from the corresponding author upon reasonable request.

Keywords: Density Functional Calculations · Fe_3O_4 · O_2 Activation · Single-Atom Catalysis · Surface Action Spectroscopy

[1] *Handbook of Heterogeneous Catalysis* (Eds.: G. Ertl, H. Knözinger, F. Schüth, J. Weitkamp), Wiley-VCH, Weinheim, **2008**.
[2] R. Lang, X. Du, Y. Huang, X. Jiang, Q. Zhang, Y. Guo, K. Liu, B. Qiao, A. Wang, T. Zhang, *Chem. Rev.* **2020**, *120*, 11986–12043.
[3] B. Qiao, A. Wang, X. Yang, L. F. Allard, Z. Jiang, Y. Cui, J. Liu, J. Li, T. Zhang, *Nat. Chem.* **2011**, *3*, 634–641.
[4] C. T. Campbell, J. R. V. Sellers, *Faraday Discuss.* **2013**, *162*, 9–30.
[5] S. Hu, W.-X. Li, *Science* **2021**, *374*, 1360–1365.
[6] G. S. Parkinson, *Catal. Lett.* **2019**, *149*, 1137–1146.
[7] X. Zhou, Q. Shen, K. Yuan, W. Yang, Q. Chen, Z. Geng, J. Zhang, X. Shao, W. Chen, G. Xu, X. Yang, K. Wu, *J. Am. Chem. Soc.* **2018**, *140*, 554–557.
[8] A. J. Therrien, A. J. R. Hensley, M. D. Marcinkowski, R. Zhang, F. R. Lucci, B. Coughlin, A. C. Schilling, J.-S. McEwen, E. C. H. Sykes, *Nat. Catal.* **2018**, *1*, 192–198.
[9] L. Giordano, G. Pacchioni, J. Goniakowski, N. Nilius, E. D. L. Rienks, H.-J. Freund, *Phys. Rev. Lett.* **2008**, *101*, 026102.
[10] N. Nilius, E. D. L. Rienks, H.-P. Rust, H.-J. Freund, *Phys. Rev. Lett.* **2005**, *95*, 066101.

[11] Z. Jakub, J. Hulva, M. Meier, R. Bliem, F. Kraushofer, M. Setvin, M. Schmid, U. Diebold, C. Franchini, G. S. Parkinson, *Angew. Chem. Int. Ed.* **2019**, *58*, 13961–13968; *Angew. Chem.* **2019**, *131*, 14099–14106.
[12] Z. Peng, B. Di, W. Li, D. Liu, X. Wen, H. Zhu, H. Song, Y. Zhang, C. Yin, X. Zhou, K. Wu, *Angew. Chem. Int. Ed.* **2020**, *59*, 14321–14325; *Angew. Chem.* **2020**, *132*, 14427–14431.
[13] Z. Liang, S. Zhang, X. Li, T. Wang, Y. Huang, W. Hang, Z. Yang, J. Li, Z. Tian, *Sci. Adv.* **2017**, *3*, eaaq1059.
[14] Y. Liu, Z. Wu, M. Naschitzki, S. Gewinner, W. Schöllkopf, X. Li, J. Paier, J. Sauer, H. Kuhlenbeck, H.-J. Freund, *J. Am. Chem. Soc.* **2020**, *142*, 2665–2671.
[15] Z. Wu, A. Płucienik, Y. Liu, M. Naschitzki, W. Wachsmann, S. Gewinner, W. Schöllkopf, H. Kuhlenbeck, H.-J. Freund, *Rev. Sci. Instrum.* **2018**, *89*, 083107.
[16] Z. Wu, A. Płucienik, F. E. Feiten, M. Naschitzki, W. Wachsmann, S. Gewinner, W. Schöllkopf, V. Staemmler, H. Kuhlenbeck, H.-J. Freund, *Phys. Rev. Lett.* **2017**, *119*, 136101.
[17] Y. Liu, Z. Wu, H. Kuhlenbeck, H.-J. Freund, *Chem. Rec.* **2021**, *21*, 1270–1283.
[18] F. Mirabella, M. Müllner, T. Touzalin, M. Riva, Z. Jakub, F. Kraushofer, M. Schmid, M. T. M. Koper, G. S. Parkinson, U. Diebold, *Electrochim. Acta* **2021**, *389*, 138638.
[19] F. Dionigi, P. Strasser, *Adv. Energy Mater.* **2016**, *6*, 1600621.
[20] R. Bliem, E. McDermott, P. Ferstl, M. Setvin, O. Gamba, J. Pavelec, M. A. Schneider, M. Schmid, U. Diebold, P. Blaha, L. Hammer, G. S. Parkinson, *Science* **2014**, *346*, 1215–1218.
[21] Z. Novotný, G. Argentero, Z. Wang, M. Schmid, U. Diebold, G. S. Parkinson, *Phys. Rev. Lett.* **2012**, *108*, 216103.
[22] J. Hulva, M. Meier, R. Bliem, Z. Jakub, F. Kraushofer, M. Schmid, U. Diebold, C. Franchini, G. S. Parkinson, *Science* **2021**, *371*, 375–379.
[23] R. Bliem, J. Pavelec, O. Gamba, E. McDermott, Z. Wang, S. Gerhold, M. Wagner, J. Osiecki, K. Schulte, M. Schmid, P. Blaha, U. Diebold, G. S. Parkinson, *Phys. Rev. B* **2015**, *92*, 075440.
[24] P. T. P. Ryan, Z. Jakub, J. Balajka, J. Hulva, M. Meier, J. T. Küchle, P. J. Blowey, P. Kumar Thakur, C. Franchini, D. J. Payne, D. P. Woodruff, L. A. Rochford, F. Allegretti, T.-L. Lee, G. S. Parkinson, D. A. Duncan, *Phys. Chem. Chem. Phys.* **2018**, *20*, 16469–16476.
[25] Earl M. Davis, K. Zhang, Y. Cui, H. Kuhlenbeck, S. Shaikhutdinov, H.-J. Freund, *Surf. Sci.* **2015**, *636*, 42–46.
[26] G. S. Parkinson, *Surf. Sci. Rep.* **2016**, *71*, 272–365.
[27] B. Arndt, R. Bliem, O. Gamba, J. E. S. van der Hoeven, H. Noei, U. Diebold, G. S. Parkinson, A. Stierle, *Surf. Sci.* **2016**, *653*, 76–81.
[28] Z. Jakub, J. Hulva, P. T. P. Ryan, D. A. Duncan, D. J. Payne, R. Bliem, M. Ulreich, P. Hofegger, F. Kraushofer, M. Meier, M. Schmid, U. Diebold, G. S. Parkinson, *Nanoscale* **2020**, *12*, 5866–5875.
[29] P. A. Redhead, *Vacuum* **1962**, *12*, 203–211.
[30] M. M. Montemore, M. A. van Spronsen, R. J. Madix, C. M. Friend, *Chem. Rev.* **2018**, *118*, 2816–2862.
[31] C. Yang, X. Yu, S. Heißler, P. G. Weidler, A. Nefedov, Y. Wang, C. Wöll, T. Kropp, J. Paier, J. Sauer, *Angew. Chem. Int. Ed.* **2017**, *56*, 16399–16404; *Angew. Chem.* **2017**, *129*, 16618–16623.
[32] M. Che, A. J. Tench, *Adv. Catal.* **1983**, *32*, 1–148.
[33] Y. Liu, Y. Peng, M. Naschitzki, S. Gewinner, W. Schöllkopf, H. Kuhlenbeck, R. Pentcheva, B. R. Cuenya, *Angew. Chem. Int. Ed.* **2021**, *60*, 16514–16520; *Angew. Chem.* **2021**, *133*, 16650–16656.
[34] R. F. W. Bader, *Acc. Chem. Res.* **1985**, *18*, 9–15.
[35] H. Gu, X. Liu, X. Liu, C. Ling, K. Wei, G. Zhan, Y. Guo, L. Zhang, *Nat. Commun.* **2021**, *12*, 5422.
[36] E. W. McFarland, H. Metiu, *Chem. Rev.* **2013**, *113*, 4391–4427.

Manuscript received: February 16, 2022
Accepted manuscript online: May 3, 2022
Version of record online: May 19, 2022